# ZnO nanowires/YAG:Ce functional heterostructure coatings with tunable optical properties

Nehed Amara, Aubry Martin, Audrey Potdevin, David Riassetto, Mouna Messaoud, François Réveret, Geneviève Chadeyron, Michel Langlet

# ZnO nanowires/YAG:Ce functional heterostructure coatings with tunable optical properties

Nehed Amara[a,b,c], Aubry Martin[a,b], Audrey Potdevin[b]*, David Riassetto[a], Mouna Messaoud[c], François Réveret[d], Geneviève Chadeyron[b] and Michel Langlet[a]

[a]*Univ. Grenoble Alpes, CNRS, Grenoble INP ◆, LMGP, 38000 Grenoble, France*
*◆ Institute of Engineering Univ. Grenoble Alpes.*
[b]*Université Clermont Auvergne, CNRS, SIGMA Clermont, ICCF, F-63000 Clermont–Ferrand, France.*
[c]*Laboratoire de Chimie Industrielle, Ecole Nationale d'Ingénieur de Sfax, Université de Sfax, Route de Soukra Km 4, 3038 Sfax, Tunisie*
[d]*Université Clermont Auvergne, CNRS, SIGMA Clermont, Institut Pascal, F-63000 Clermont–Ferrand, France.*
**corresponding author : audrey.potdevin@sigma-clermont.fr, +33 (00)473 407 607*

Luminescent ZnO nanowires (NWs)/YAG:Ce heterostructure coatings have been elaborated by impregnating cheap hydrothermally-grown ZnO NWs array with ground commercial YAG:Ce nanoparticles (NPs). TEM and photoluminescence quantum yield measurements have been used to make YAG:Ce NPs suitable for soaking within the ZnO NWs. Structural, morphological and optical studies of functional nanocomposite coatings have evidenced an optimal amount of YAG:Ce allowing the visible photoluminescence signal of ZnO NWs nearly to triple whereas slight red shift accompanied by an enlargement of the long wavelength side has been observed for YAG:Ce emission. These phenomena have been explained through the existence of structural defects on ZnO NWs surface and on emission mechanisms implying either scattering effects or the passivation of NWs surface by YAG:Ce NPs. Furthermore, an energy diagram involving different structural defects of ZnO NWs as well as $Ce^{3+}$ ions energy levels has been built from excitation and emission spectra and from decay curves recorded monitoring the orange-red emission of ZnO. The elaborated heterostructure functional coatings have proved to exhibit tunable optical properties in terms of spectral distribution playing on the excitation source. Hence, they appear as a smart way for developing LEDs-based devices with flexible photometric parameters for a broader range of optical applications.

Keywords: functional coatings, LEDs, light extraction, phosphors, luminescent heterostructures

## INTRODUCTION

Due to their high brightness and long lifetime, White Light-Emitting Diodes (WLEDs) have gradually replaced other lighting sources such as Hg-based fluorescent devices. Currently commercialized WLEDs generally associate one or more phosphor(s), deposited in the form of coatings, to a semiconductor (SC) chip emitting in the ultraviolet or blue wavelength region. On-chip or remote phosphor configurations are usually employed for the luminescent coatings [1]. Even if WLEDs-based display and lighting devices exhibit good photometric parameters, their performances in terms of external quantum efficiency and service life can be further improved [2-4]. This latter could be lengthened thanks to a better thermal dissipation whereas the former relies on both Internal Quantum Efficiency (IQE) and Light-Extraction Efficiency (LEE), which represents the ratio between the number of photons extracted to the air and the number of photons generated in the active layer [2, 4, 5]. Actually, the emitted light is hard to extract into the air since

there is a gap between the high refractive index of the phosphor (n~1.8 for the most common used $Y_3Al_5O_{12}:Ce^{3+}$ − YAG:Ce phosphor) and the air (n~1). Then, the device suffers from a loss of light because a large fraction of the produced photons are backscattered to the chip or trapped in dielectric structures inherent to the substrate (luminescent coatings) due to Total Internal Reflection (TIR) and the presence of a waveguide mode [5-7]. Several approaches have been reported to boost LEE value. They are generally based on the increase in the escape probability of photons, giving them more chances to find the escape cone defined by $\theta_C = \sin^{-1}(\frac{n_{air}}{n_{AL}})$, $n_{air}$ and $n_{AL}$ being refractive indexes of the air and of the Active Layer (AL) (for example the phosphor) respectively [7, 8]. Among the existing light extraction management strategies based on this increase, one can cite surface roughening [4, 9], use of photonic crystals [2], nanorods or nanopillars [7] and many others. In particular, cheap and tunable [10, 11] ZnO nanostructures such as nanorods, nanopillars, nanowires and nanosheets have attracted much attention to this end over last years since they can contribute to LEDs improvement in more than one way: 1) they are characterized by a refractive index ($n_{ZnOBulk}$~2.0-2.1) intermediary between GaN-based LED (n~2.4) and air, expanding the escape cone value $\theta_C$ [12-14], 2) their high surface-to-volume ratio allows a better thermal dissipation, entailing a longer LED lifetime [14], 3) depending on their morphology and inherent structural defects, they can be used either as light waveguides [15] or to increase light scattering through surface nanotexturing [16].

On the other hand, ZnO has also been studied over the last decade as a full-fledged phosphor to serve either as a UV excitation source [17], or, thanks to the various structural defects it can contain, as a blue-white phosphor suitable for near-UV LEDs ($\lambda_{exc}$ lying in 360-380 nm range). Indeed, these defects (oxygen or zinc vacancies and interstitials) give rise to photoluminescence in different wavelength domains of the visible spectrum (from 400 to 750 nm). By playing on their quantity, one can reach a close white output [11, 18, 19] when excited by near-UV LEDs. Besides, these optical properties can be slightly modified by doping ZnO with other metals such as Co, Cu, Fe…[19, 20].

If they have already been used to improve emission efficiency or quality of GaN-based LEDs [12, 14, 16], ZnO nanostructures have scarcely been combined with phosphors to yield an enhanced white light, whether in terms of light extraction or in terms of photometric parameters [3, 21]. However, they could successfully be used for this latter issue thanks to their tuneable emission profile [11]. Indeed, to improve the Color Rendering Index (CRI) of the current commercial white LEDs, red phosphors are generally added to the blue LED chip and YAG:Ce combination [22]. These red phosphors must fulfil several requirements such as a good stability upon photonic and thermal stresses in addition to a high emission quantum yield. Sulfides and nitrides doped with $Eu^{2+}$ are generally used as red emitting phosphors in commercial lamps [22, 23] although they suffer from several drawbacks such as poor thermal stability, water sensitivity or high cost. Recently, new rare-earth free phosphors have been developed as alternative red source suitable for blue or near-UV LEDs [24, 25]. ZnO, as cheap and rare-earth free compound, could be included in this category.

In this work, we have chosen to use the multiple properties and potentialities of ZnO nanostructures to elaborate nanocomposite functional coatings combining hydrothermally-growth ZnO nanowires (NWs) with YAG:Ce nanoparticles (NPs). The original goal was twofold: 1) to increase the photoluminescence efficiency of YAG:Ce coatings thanks to physical phenomena related to ZnO NWs (waveguiding or scattering effect), 2) to improve the spectral distribution of the YAG:Ce coatings by providing a red

component without any supplementary rare-earth doped phosphor. It is noteworthy that main reports existing on the combination between YAG:Ce and ZnO were dedicated to the enhanced photocatalytic activity of the elaborated heterostructures [26, 27]. They did not deal with their potential applications in LEDs-based devices. Only Chao *et al.*[28] studied the effect of surface coating of YAG:Ce microparticles with ZnO nanoparticles, highlighting an increase in emission intensity of YAG:Ce in the presence of ZnO under blue excitation that they ascribed to a reduction in surface defects. No change in emission profile was observed and no photoluminescence mechanism was discussed.

Since optical properties of ZnO NWs are greatly dependent on their elaboration conditions [11, 29], our present work was built on a robust and well-mastered synthesis procedure detailed in previous works [30-32] involving a sol-gel derived seed layer. Meanwhile, YAG:Ce NPs suspension was elaborated through an optimized ball-milling process. Then, these NPs were used to soak ZnO NWs through a multi-coating step to lead to ZnO NWs/YAG:Ce nanocomposite functional coatings. The structural and morphological properties of ZnO alone, YAG:Ce alone and the heterostructures were studied by means of standard methods (mainly XRD, TEM and SEM). Quantum yield of ground YAG:Ce powders were determined and photoluminescence measurements allowed to record excitation and emission spectra of each kind of material. Interactions between $Ce^{3+}$ ions in YAG matrix and ZnO NWs were tentatively unraveled based on energy diagrams and a schematic representation of photon paths within the composite structure was suggested to explain the encountered optical behaviours.

# 1. EXPERIMENTAL SECTION

## 1.1. Elaboration of ZnO nanowires

ZnO seed layers were deposited using a sol-gel approach detailed in our previous work [30]. Briefly, a sol was prepared by diluting zinc acetate dihydrate (ZAD) and monoethanolamine (MEA) in 1-butanol with a ZAD concentration and a ZAD/MEA molar ratio fixed at 0.32 M and 1, respectively. After 3 h stirring at 90°C, a clear sol was obtained. Subsequently, a 300 µL droplet of the sol was deposited by spin-coating at 3000 rpm on 3 × 3 cm2 (100) silicon substrates. The obtained xerogel films were then annealed at 540°C for 1h under air, leading to crystalline ZnO thin films. No reliable XRD pattern could be recorded on the seed layer owing to its very weak thickness estimated to be less than 10 nm. However, previous studies performed on thicker layers obtained through a multi-deposition procedure showed that the layers were well crystallized with a moderate c-axis orientation, i.e. a texture coefficient around 60% (to be compared with values of 33 and 100% for randomly or totally c-axis oriented samples, respectively). Finally, so-obtained seed layers were cleaned with an oxygen plasma at a power of 12 W for 4 min to favor the subsequent growth of ZnO NWs.

In a second step, ZnO NWs were grown on the seed layers by hydrothermal synthesis at ambient pressure according to our previously published procedure [31]. The 3 × 3 $cm^2$ ZnO/Si sample was fixed with a 45° tilt angle on a Teflon sample holder. Meanwhile, ZNH and HMTA were mixed at room temperature in 100 mL of deionized water with ZnH and HMTA concentrations of 25 mM. This mixture was stirred for 1 min and it was then heated up to 90°C using a hot plate equipped with an automatic temperature regulation system. The sample holder (with substrate) was then immersed in the heated solution for 30 min, the coated side of the substrate

being oriented downwards, in order to achieve growth of the NWs. After that, samples were rinsed with deionized water and then dried with a nitrogen stream.

## 1.2. Grinding of commercial YAG:Ce phosphor

YAG:Ce nanoparticles (NPs) suspension was obtained *via* wet grinding method from a commercial YAG:Ce powder (PhosphorTech QMK 58/F-U1) using a high-energy ball grinder (Emax, Retsch GmbH) without any surfactant. Grinding conditions have been optimized to produce particles small enough to be efficiently incorporated between ZnO NWs. A powder to ball weight ratio of approximately 4 % has been used throughout this study and absolute ethanol was used as a solvent. As grinding media, yttria-stabilized $ZrO_2$ (YSZ) grinding beads (Retsch) with a diameter of 0.1 or 0.5 mm have been used. Their quality has been chosen to prevent any phosphor contamination by YSZ phase. Approximately 96 g of grinding beads have been introduced into the grinding jar (total volume 50 mL) for 4 g of YAG:Ce powder. The speed was set at 1800 rpm and the process temperature has been adjusted using an internal thermostat which prevents temperature to exceed 70°C. Different milling times have been considered (15, 30 and 45 min) and a milling time of 30 min has been used to compare the effect of the beads diameter.

After grinding, a known volume of YAG:Ce NPs suspensions was dried overnight at 80°C to assess their mass concentration and to perform structural analyses. This assessment has been carried out on several samples. Since the obtained mass concentration of NPs suspensions was estimated too high for an efficient impregnation of ZnO NWs, precise volumes of absolute ethanol were added to reach a mass concentration of 20 g/L. Sonication was then used to improve both NPs dispersion in ethanol and their size distribution. Size distribution and zeta potential of optimized stable YAG:Ce NPs suspensions (sonicated or not) were studied by zetametry, which allowed to define the best conditions of sonication: 30 s at 40% of maximum probe intensity (Figure S1 in supplementary informations/SI). This top-down approach has been privileged compared to bottom-up ones (glycothermal synthesis of YAG:Ce NPs for example) mainly because of the poor emission efficacy obtained through these latter (external quantum yield between 5 and 15%) [33].

## 1.3. Elaboration of nanocomposite functional coatings

Nanocomposite coatings were elaborated using spin-coating method. A 300 µL droplet of the YAG:Ce NPs suspension (20 g/L) was deposited at 3000 rpm on 3 × 3 $cm^2$ ZnO NWs coatings with a drying time of 1 min at room temperature to evaporate the solvent. Several samples were elaborated by varying the number of depositions onto the ZnO NWs coatings: 5, 10, 15 and 20 cycles were carried out. A coating made only of YAG:Ce (10 depositions) and a ZnO NWs coating (without YAG:Ce) were used as reference samples.

## 1.4. Characterization techniques

The X-ray diffraction (XRD) patterns of all samples were obtained with a Philips Xpert Pro diffractometer operating with the Cu-$K\alpha_1$ radiation ($\lambda$= 1.5406 Å). Transmission Electronic Microscopy (TEM) images were recorded on a Hitachi H-7650 microscope at the Centre Imagerie Cellulaire Santé (CICS) of Clermont-Ferrand. Top views scanning electron microscope (SEM) images were

collected at 2MAtech (Clermont-Ferrand) under high vacuum using a ZEISS Supra 55 FEG-VP instrument operated at 3kV and cross sectional SEM images were collected at LMGP using an Environmental FEI QUANTA 250 instrument operated at 20kV.

Zeta potentials (ζ) were measured by laser Doppler electrophoresis (Zetasizer NanoZS, Malvern, UK). The dilute alcoholic suspensions were also studied in terms of particle size distribution using the dynamic light scattering (DLS) principle, available in the same instrument used for zeta potential determinations.

Raman spectra were recorded with a T64000 Jobin-Yvon confocal micro-Raman spectrograph. The confocal configuration of the micro-Raman instrument allows depth profiling of the samples, permitting the detection of the Raman spectrum from a volume as small as 1 $\mu m^3$ focusing at different depths into the sample. The excitation source used was the 514.5 nm wavelength line from a Coherent model 70C5 $Ar^+$ laser operating at a power of 200 mW. A 50-fold objective lens was used for the focusing and the data was collected for 2×75 s. The resolution on the wavenumbers is approximately 1 $cm^{-1}$.

The optical properties were investigated by recording the photoluminescence spectra with a Jobin-Yvon set-up consisting of a Xenon lamp operating at 400 W and two monochromators (Triax 550 and Triax 180) combined with a cryogenically cold charge coupled device (CCD) camera (Jobin-Yvon Symphony LN2 series) for emission spectra and with a Hamamatsu 980 photomultiplicator for excitation ones. For ZnO NWs coatings and ZnO NWs/YAG:Ce composite coatings, emission spectra were recorded in different areas of the samples to control the homogeneity of the optical performances. Presented data are thus representative of the studied samples.

Quantum yields (QY) efficiencies were assessed using C9920−02G PL-QY measurement system from Hamamatsu. The setup comprised a 150W monochromatized Xe lamp, an integrating sphere (Spectralon Coating, Ø = 3.3 inch) and a high sensitivity CCD spectrometer for detecting the whole spectral luminescence. All luminescence experiments were performed at room temperature.

Time resolved photoluminescence (TRPL – decay times) measurements were performed at room temperature. The excitation line was the third harmonic of a Ti:Sa pulsed laser (375 nm) with a pulse duration of 150 fs and a repetition rate of 76 MHz. The emission of the samples was spectrally resolved using a 320 mm focal length monochromator and the time resolved signal was measured using a streak camera.

# 2. RESULTS AND DISCUSSION

## 2.1. Structural and morphological study of ZnO nanowires

Figure 1 displays the XRD pattern of the grown ZnO NWs (Figure 1b) compared with that obtained for the Si wafer alone (Figure 1a). Most of diffraction reflections are relative to Si substrates but several reflections observed in Figure 1b can also be assigned to the hexagonal structure (wurtzite) of ZnO ((002), (101), (102) and (103) planes). In particular, the peak around $2\theta$=34.8°, corresponding to the (002) plane of hexagonal ZnO, is by far the most intense whereas the main diffraction peak of ZnO is generally (101) (JCPDS file 36-1451) [34]. This suggests that ZnO NWs have a mean c-axis orientation perpendicularly to the substrate, even

if the presence of secondary reflections indicate a certain dispersion in this orientation. These results are concordant with previous works made on hydrothermally-synthesized ZnO nanorods or nanowires [17, 35, 36].

Cross sectional and top SEM views of as-grown ZnO nanowires are presented in Figure 2. Si wafers are entirely covered by a highly homogeneous array of ZnO nanowires (Figure 2(c)). Even if they are rather c-axis oriented (Figure 2(a)), the obtained NWs do not exhibit a perfect verticality, which is concordant with XRD patterns. This behavior was already observed in our previous work [31]. Here, apparent NWs are characterized by diameters ranging between 30 and 50 nm and lengths of 400-500 nm.

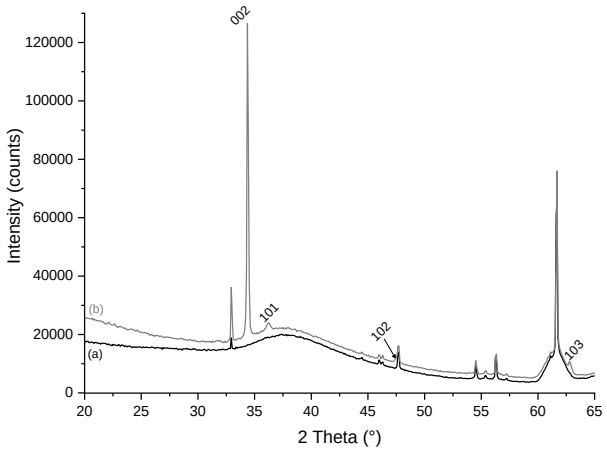


**Figure 1 : XRD patterns of (a) silicon wafer and (b) ZnO NWs grown on Si wafer.**

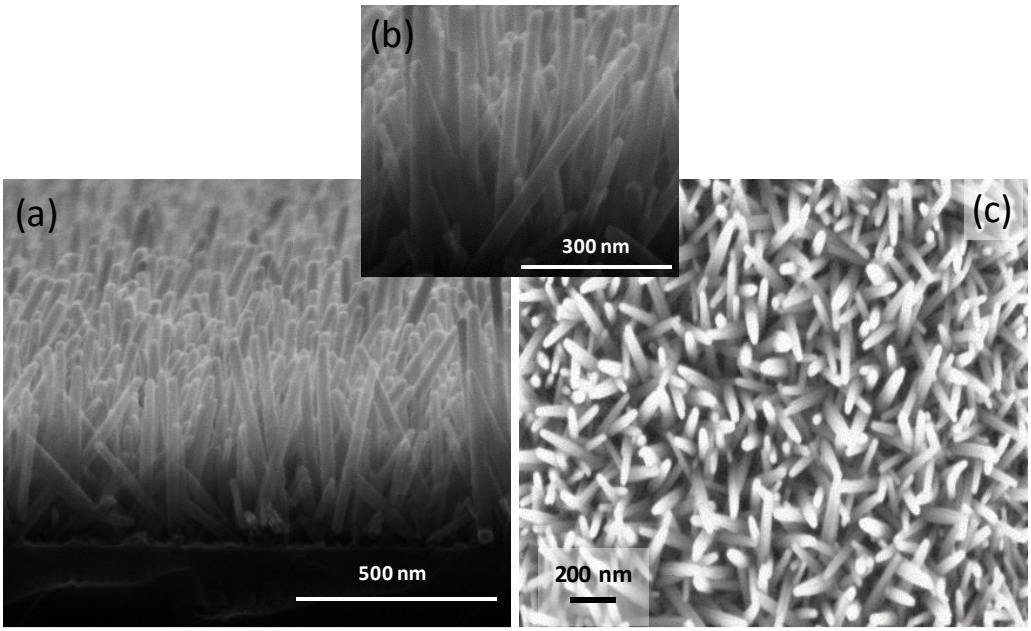


**Figure 2 : (a), (b) Cross-sectional and (c) top SEM views of the as-grown ZnO NWs.**

From Figure 2(a) and (c), the space between ZnO NWs can be estimated to be within the gamut 50-150 nm. Consequently, the target diameter for YAG:Ce NPs to insure an effective impregnation of the ZnO NWs is 50 nm or less. Grinding conditions of the commercial phosphor have been optimized to reach this target.

## 2.2. Optimization of grinding conditions

Electron microscopy has been used to study the morphological properties of original and ground commercial YAG:Ce powders. The SEM image of the commercial powder (Figure S2) shows this phosphor is characterized by highly crystalline and well facetted micro-sized particles. These particles are very dense and a large size distribution is highlighted in the range 500 nm -10 µm.

TEM images have first been recorded on powders milled for 30 min with beads of 0.5 and 0.1 mm in diameter. Results clearly evidenced that a diameter of 0.1 mm led to both average NPs diameter and size distribution more appropriate to NWs impregnation than those obtained using beads with a diameter of 0.5 mm (Figure S3). Then, grinding time was adjusted to further reduce the mean diameter and better the size distribution of derived NPs. TEM images and associated size distributions of ground NPs are presented in Figure 3. Size distributions have been determined from at least 60 measurements made on different TEM images for each sample and using Origin® software (tool "Frequency Counts"). Outcomes of TEM analysis in terms of average particle size are summarized in Figure S4 and compared to target. Considering this figure, it appears necessary to use grinding beads of 0.1 mm of diameter with a grinding duration of at least 30 minutes to favor an optimal impregnation of derived NPs.

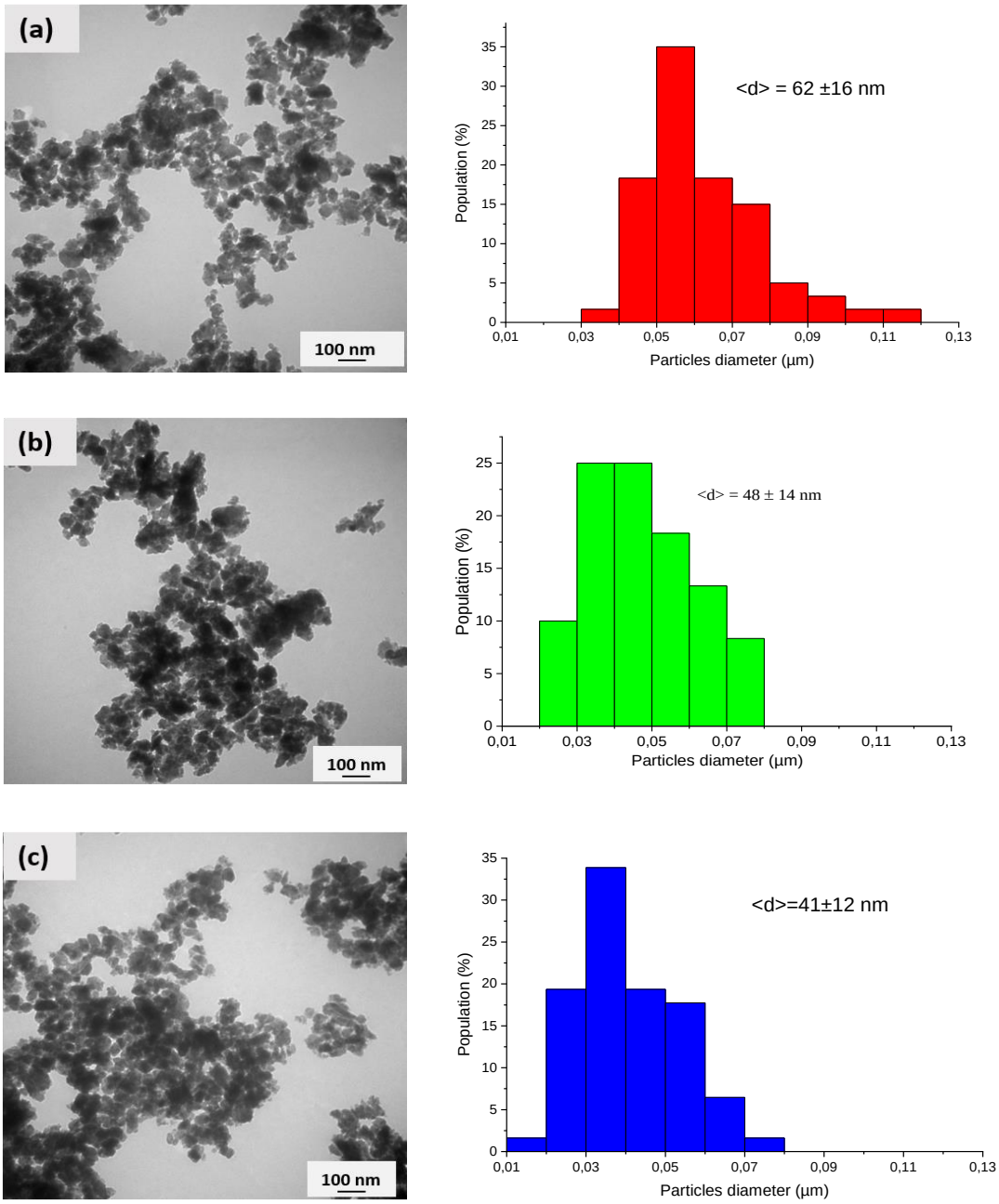


**Figure 3 : TEM images and corresponding size distribution of powders ground with 0.1 mm beads during (a) 15, (b) 30 and (c) 45 min.**

Initial commercial YAG:Ce powder and ground samples have also been studied by XRD to check the preservation of the crystalline YAG structure after ball-milling. The most intense diffraction reflections observed in the experimental XRD pattern obtained from the commercial YAG:Ce powder (Figure S5) are assigned to the YAG structure (JCPDS-file 33-0040) revealing that it mainly consists of a well crystallized YAG phase. Several weak reflections, marked with an asterisk, correspond to another unidentified phase present in low quantities. This parasitic phase is probably linked to the synthetic process used by the provider to obtain YAG. The diffraction patterns recorded on initial and ground commercial YAG:Ce powders (Figure S6) show that, whatever the grinding conditions, ground powders are characterized by a significant decrease in diffraction peaks intensity, as well as the broadening of

these peaks, as a consequence of both crystallite size reduction and milling induced defects associated with the increase in internal stress. This trend is amplified when using smaller milling beads (0.1 mm instead of 0.5 mm) whereas, for beads of 0.1 mm of diameter, the grinding duration does not appear to have a significant impact on diffraction peaks intensity and broadness. These changes in diffraction patterns with ball-milling have already been reported for different ceramics ($Al_2O_3$ [37], $Si_3N_4$ [38], ZnO [39]) and notably for phosphors such as $SrAl_2O_4$ :$Eu^{2+}$, $Dy^{3+}$ [40], $Eu^{2+}$ and $Dy^{3+}$ doped strontium aluminate phosphors [41] or SrS :$Ce^{3+}$ [42]. It is noteworthy that very few studies have explored the top-down approach we present here, starting directly from a commercial phosphor [40]. It can be noticed that no trace of YSZ phase has been observed for ground powders which testifies to the grinding beads quality (no phosphor pollution).

Photoluminescence external quantum yields of both initial and ground YAG:Ce powders have been measured tuning the excitation in the 270-500 nm range. The spectra of Figure 4 (left part – 4(a)-(e)) show the same overall shape for all the samples, i.e. two large bands having maxima located around 340 and 457 nm. They are due to the electron transitions from the ground-state $^2F_{5/2}$ of $Ce^{3+}$ ions to the different crystal field splitting components of their 5d excited state in YAG matrix [43, 44]. The more intense peak located at 457 nm matches very well the blue emission of GaN-based LED; it is the reason why crystallized YAG:$Ce^{3+}$ powders represent the most used phosphor in white GaN-based LEDs [45]. It can be observed that quantum yield is higher for initial YAG:Ce powder, whatever the excitation wavelength. After grinding, a drop in external quantum yields occurs which is directly related to the amorphization of milled samples evidenced by XRD and to grinding induced surface defects [39, 42]. Indeed, such defects are well-known to act as luminescence quenchers [46]. It is interesting to notice that i/ for a same grinding duration of 30 min, a bead diameter reduction results in a significant decrease in the quantum yield which is correlated to a more efficient grinding, as illustrated in Figure 3, while ii/ an increase in grinding duration has very slight influence on photoluminescence quantum yield for powders ground with 0.1 mm beads (Figure 4(c)-(e)) whereas the longer this duration is, the sharper size distribution becomes, as shown in Figure 3.

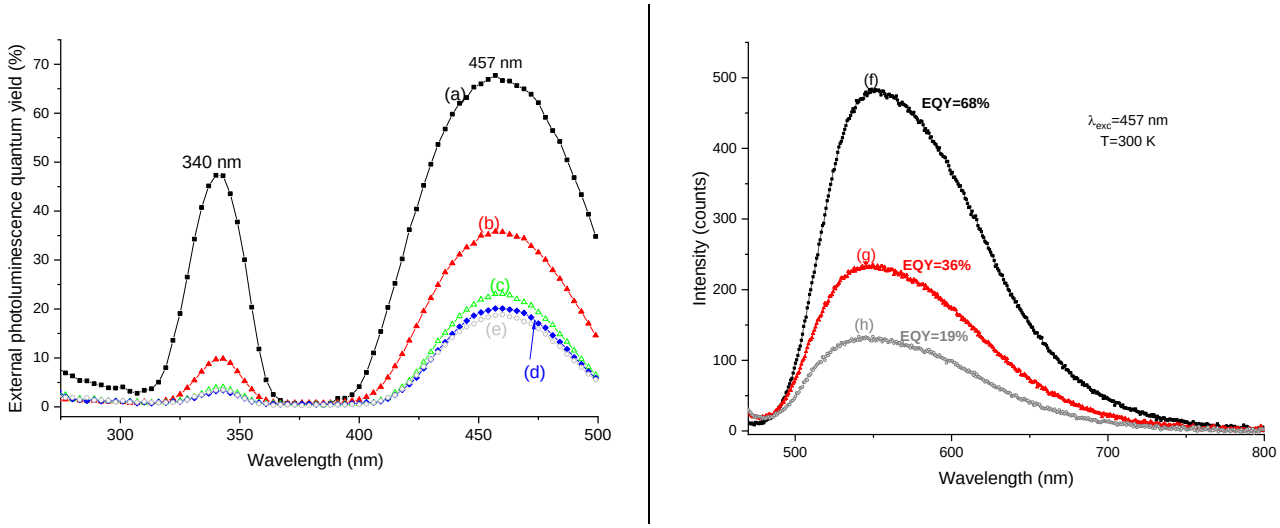


**Figure 4 : Left - Evolution of the room temperature photoluminescence quantum yield versus excitation wavelength for commercial YAG:Ce before (a) and after grinding with various bead diameters / grinding durations: (b) 0.5 mm/30 min, (c) 0.1 mm/15 min, (d) 0.1 mm/30 min and (e) 0.1 mm/45 min. Right - Emission spectra of commercial YAG :Ce under**

**excitation à 457 nm before (f) and after grinding using different grinding bead diameters / grinding durations: (g) 0.5 mm/30 min and (h) 0.1 mm/45 min.**

Emission spectra of initial commercial phosphor and some ground powders are gathered in Figure 4 (right part – 5(f)-(h)). Every emission spectrum consists of a wide band in the green-yellow range corresponding to the electron transitions from the lowest crystal-field splitting component of the 5d level to the ground state of $Ce^{3+}$ split in $^2F_{5/2}$ and $^2F_{7/2}$ levels [43]. Initial phosphor logically displays higher external quantum yield (EQY of about 68 % upon 457 nm excitation – Figure 4f ) compared to its ground counterparts (EQY = 36 % and 19% for beads diameter of 0.5 and 0.1 mm, respectively), mainly due to its higher crystallinity (as shown by XRD patterns) and less internal stress and surface defects [39, 40]. For the same reasons, powders ground with bigger beads also exhibit a higher EQY (Figure 4(g)) than those more efficiently ground with smaller beads (Figure 4(h)). A slight blue-shift is also observed between initial phosphor, for which the maximum of emission intensity is located at 550 nm, and the ground powders characterized by emission lines around 545 nm. This can be ascribed to quantum confinement or surface influence accompanying the particle size reduction evidenced by TEM [39, 42, 47].

Based on the afore presented results concerning morphological, structural and optical properties of ground powders, we decided to use for ZnO NWs impregnations the powder ground during 45 min with 0.1 mm beads which met the specification concerning the targeted diameter (<d>=42 ±12 nm). Longer milling times have not been considered since they would have resulted in less efficient phosphors whereas the decrease in the average size and size distribution width would certainly have not been significant compared to a milling time of 45 min.

## 2.3. Structural and morphological study of composites

Structural properties of composite coatings have been studied by XRD. Obtained patterns (Figure 5(a), (b) and (c) – left part) suggest a change in NWs orientation when they are impregnated with YAG:Ce suspension. In particular, a remarkable decrease in the intensity of the diffraction reflection corresponding to (002) plane ($2\theta$=34.8°) of ZnO compared to (101) plane is observed after deposition of YAG:Ce suspension. This decrease is already appreciable after 5 coatings, and it is further amplified after 20 YAG:Ce coatings. Furthermore, some diffraction planes of ZnO, which were barely noticeable in the absence of YAG:Ce, have their intensity boosted when 20 coatings of YAG:Ce suspension have been carried out, in particular the (100) plane at $2\theta$=31.8° (Figure 5(c) – right part). These changes could be related to a loss of verticality of ZnO NWs.

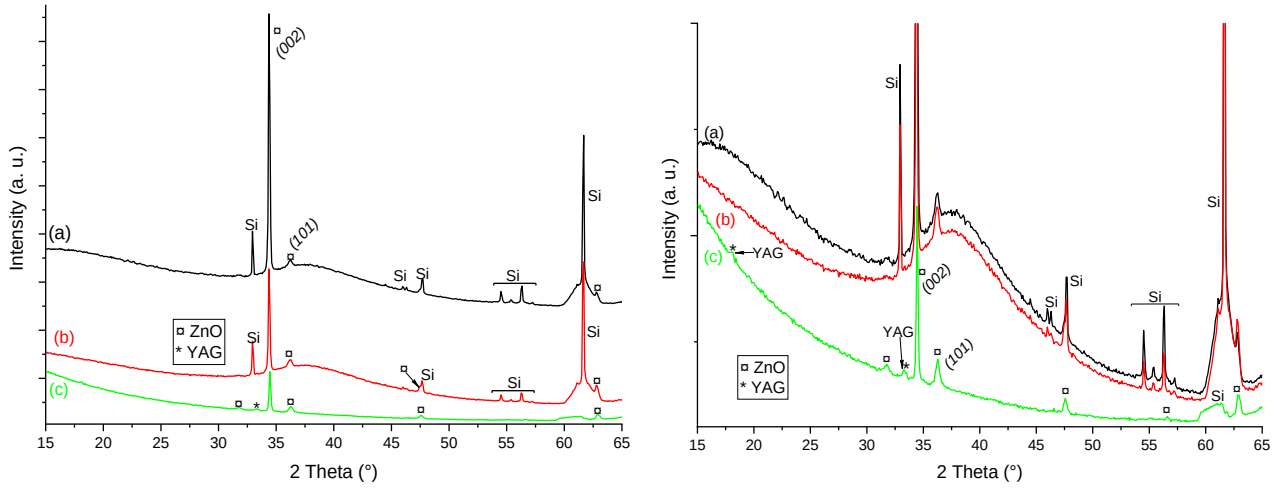


**Figure 5 : Left: XRD patterns of (a) ZnO NWs alone and ZnO/YAG:Ce composite coatings made with (b) 5 and (c) 20 impregnations of YAG:Ce NPs suspension (Y offset has been used to better see the top of the most intense diffraction reflection) ; Right: Corresponding zoom-in (no Y offset used). Reflections of the Si substrate and YAG phase are indicated in the figure, and those of the ZnO component are indexed.**

At the same time, diffraction signals related to Si wafer almost disappeared. Finally, two of the main diffraction reflections of YAG phase can be observed at 2θ=18.1°, 2θ=33.3° when 20 coatings of YAG:Ce have been carried out (Figure 5(c) – right part). Their intensity is very weak due to the lack of crystallinity of ground powders associated with a small quantity of YAG:Ce compared to the highly crystalline ZnO NWs. With only 5 coatings, the quantity of YAG:Ce is probably too low to be detected by XRD due also to the poor crystallinity of the ground phosphor. Morphological study of these coatings has been used to understand these results and check our assumptions.

Top-view and cross-sectional SEM images of composites ZnO/YAG:Ce obtained after several cycles of impregnations (5 to 20) are gathered in Figure 6 and Figure 7 respectively. For comparison, Figure 6 also illustrates the top-view SEM images of ZnO NWs (Figure 6(a)) and YAG:Ce NPs coatings alone (Figure 6(b)). On top-view images, one can observe that YAG:Ce NPs well fulfill spaces between ZnO NWs after 5 (Figure 6(c)) and 10 impregnations (Figure 6(d)). After 15 impregnations (Figure 6(e)), some NWs start to disappear, showing that additional YAG:Ce NPs aggregates are formed at their surface leading to the birth of a surface crust. This phenomenon is further amplified on the sample made with 20 impregnations, showing a predominance of the surface crust. These data illustrate therefore a competition between NWs impregnation and surface crust formation, this latter mechanism being intensified when the number of YAG:Ce NPs coatings increases. We should note that this surface crust does not preclude to observe ZnO diffraction reflections on the XRD pattern (Figure 5(c)) but it is probably responsible for the near disappearance of Si wafer ones.

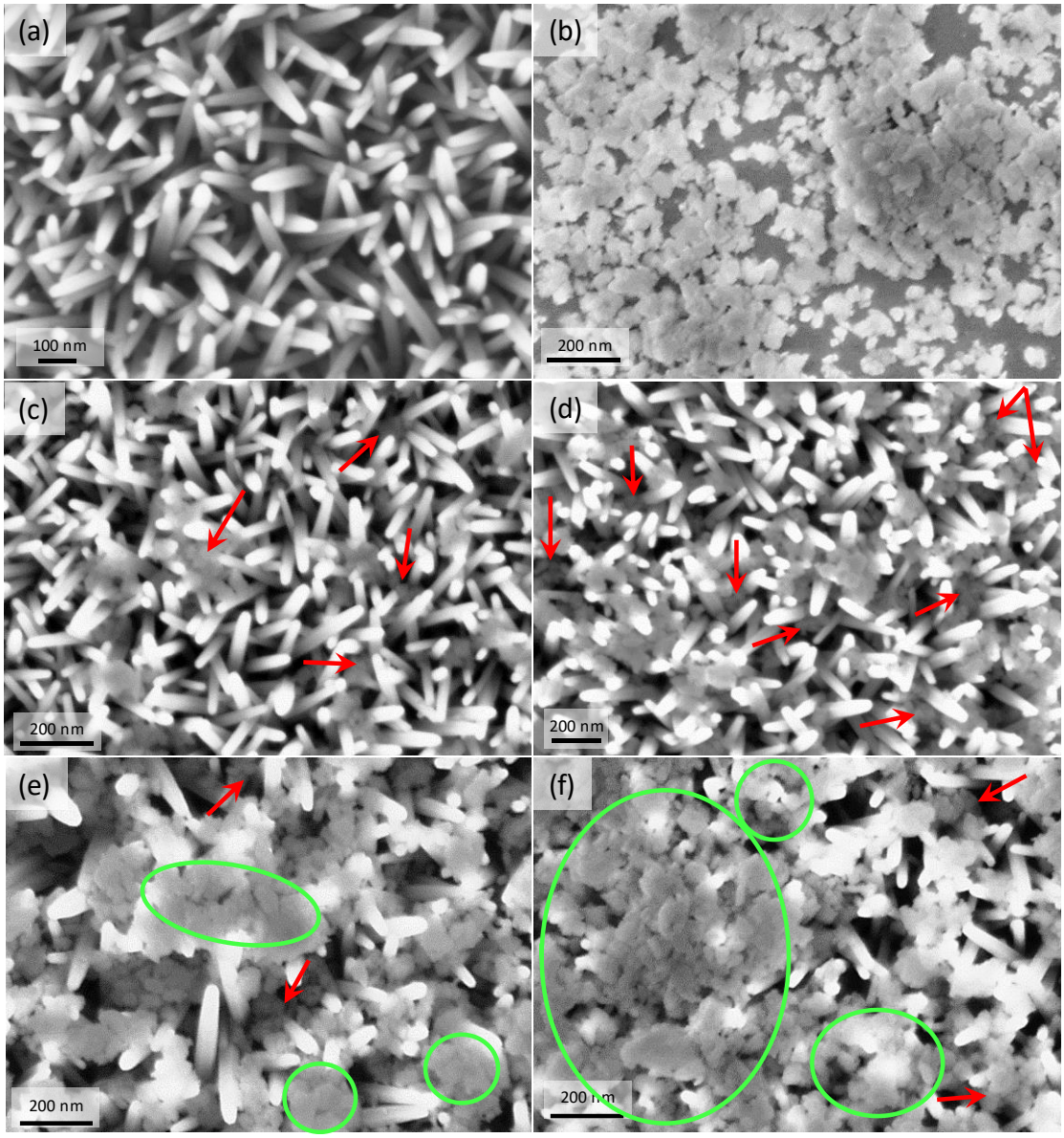


**Figure 6 : SEM images of (a)ZnO NWs alone, (b) YAG:Ce alone (10 coatings of 20 g/L ground YAG:Ce suspension) and ZnO/YAG:Ce composite coatings made with (c)5, (d)10, (e)15 and (f) 20 impregnations of YAG:Ce NPs suspension. In (c) to (f), red arrows indicate YAG:Ce NPs lying between ZnO NWs whereas green circles highlight the surface crust.**

Previous observations are confirmed by cross-sectional SEM images. In Figure 7(a), when compared with cross-sectional views of NWs alone (Figure 2), some NWs start to disappear after 5 NPs impregnations, showing that YAG:Ce NPs have partially fulfilled spaces between the NWs. This feature is further amplified after 20 impregnations (Figure 7(b)) together with the formation of additional surface features that illustrate the formation of a thick YAG:Ce crust. This crust explains in particular why the diffraction reflections due to the Si substrate almost disappear after 20 impregnations (Figure 5(c)). Besides, one can see that the verticality of the ZnO NWs decreases after 5 impregnations compared to that of bare NFs, and this decrease is noticeably heightened after 20 impregnations. This behavior, which is concordant with the loss of verticality evidenced by XRD (Figure 5), has not been clearly

explained. It might arise from both stress effects induced by a growing amount of NPs impregnated in-between the NWs and the force caused by the nanoparticles' weight.

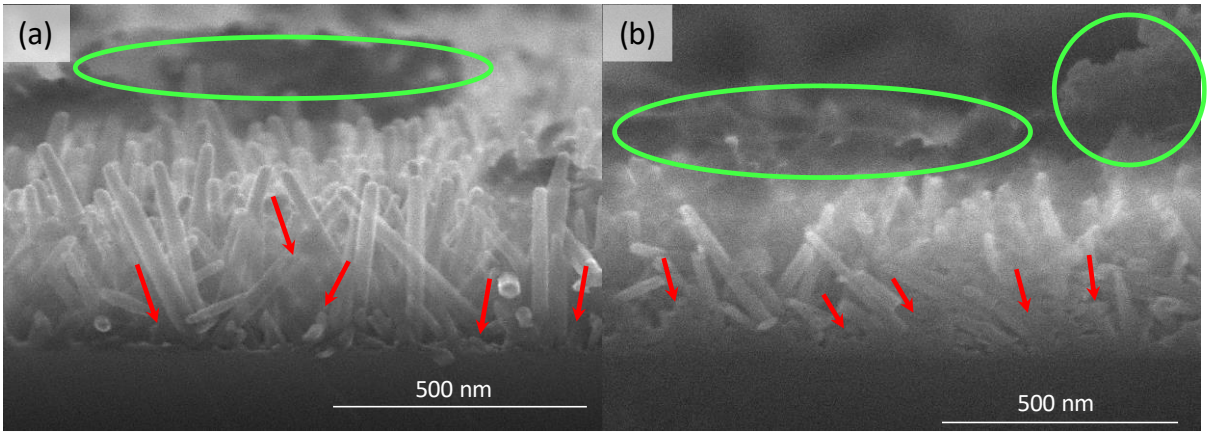


**Figure 7 : Cross-sectional SEM images of ZnO/YAG:Ce composite coatings made with (a)5 and (b) 20 impregnations of YAG:Ce NPs suspension. Red arrows indicate YAG:Ce NPs lying between ZnO NWs whereas green circles highlight the surface crust.**

## 2.4. Optical characterization of composites

Room temperature excitation spectra ($\lambda_{em}$=610 nm) have been recorded and are gathered in Figure 8. For ZnO NWs alone (Figure 8(a)), excitation spectrum presents a distinct absorption edge around the wavelength corresponding to the band gap energy of ZnO around 3.35-3.38 eV (367-369 nm). The onset of this edge can be extrapolated to be at ~3.14 eV (395 nm). No significant excitation signal appears in the visible range. This excitation profile is almost concordant with the few PLE spectra monitoring the orange emission found in the literature [29, 48, 49]. The major difference is the slight decrease in excitation signal at higher energies which has already been observed on ZnO particles but monitoring the green luminescence [34]. On the excitation spectrum recorded for the YAG:Ce coating (Figure 8(b)), the main absorption bands of YAG:Ce phase are well observed around 330 and 460 nm, corresponding to the electron transitions $^2F_{5/2} \rightarrow {}^2D_{5/2}$ and $^2F_{5/2} \rightarrow {}^2D_{3/2}$ of $Ce^{3+}$ ions, respectively [44, 50]. The composite is characterized by a combination of both excitation spectra with two primary excitation signals located around 370 and 460 nm (Figure 8(c)). Let us add that the energy threshold corresponding to ZnO NWs remains similar (no change in the onset) which may indicate that the presence of YAG:Ce has no influence on the energy level of shallow defects and does not induce any sub-band gap states [34]. However, in an intriguing way, the absorption decreases at higher energies which we had not been able to explain.

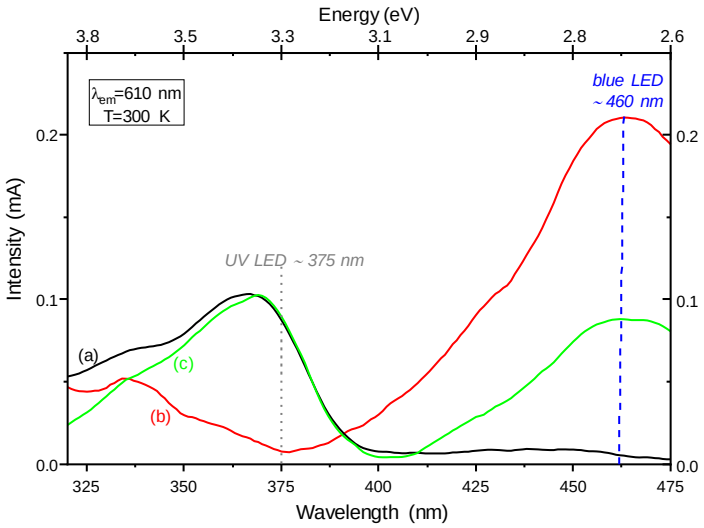


**Figure 8 : Room temperature excitation spectra of (a) ZnO NWs alone, (b) YAG:Ce alone (10 coatings of 20 g/L ground YAG:Ce suspension) and (c) ZnO/YAG:Ce composite made with 10 impregnations of YAG:Ce NPs suspension.**

The excitation profile obtained for the composite coating means that this multimaterial architecture can be efficiently excited at either UV or blue wavelengths similar to those produced by commercial near-UV or blue LEDs, respectively. Consequently, emission spectra have been recorded upon both near-UV and blue excitations.

Room temperature emission spectra are shown in Figure 9. Upon blue excitation (457 nm),the only weak signal presented around 480 nm for ZnO NWs alone may arise from the excitation source (Figure 9(a)). Emission spectra recorded for composites with various YAG:Ce amounts present a profile close to the one obtained for YAG:Ce alone. However, with closer inspection (Figure S7), it appears that the presence of ZnO NWs yields both a slight red shift of the emission maximum (from 547 to 552 nm) together with a modest enlargement the long wavelength side (about 10 nm) which could correspond to a slight contribution of ZnO NWs between 550 and 650 nm. Regarding the excitation spectrum (Figure 8) and the emission one upon 457 nm excitation (Figure 9(a)), no energy transfer from $Ce^{3+}$ ions to ZnO NWs conduction band seems to be possible. Besides, as mentioned in the introduction, very few articles concern the association of YAG:Ce and ZnO; they generally present emission spectra under UV excitation at a wavelength where both ZnO and YAG:Ce are excitable (around 325 nm) [51]. Only Liu and co-workers [26] present emission spectra of ZnO NPs – YAG:Ce NPs composites recorded under blue excitation but only to confirm the presence of YAG:Ce phosphor at the surface of their ZnO NPs. They did not compare their emission spectrum with that of YAG:Ce alone. Consequently, the observed slight enlargement of the emission profile of YAG:Ce/ZnO NWs composite has not yet been neither observed nor explained.

Figure 9(a) also shows that emission spectra of composites have their intensity increased with the number of impregnations, which is directly related to the YAG:Ce content in the composite. It should also be noted that, when comparing the emission intensity of YAG:Ce alone (10 coatings) and ZnO+YAG:Ce (10 impregnations), the composite presents a 30% lower emission intensity. However, it is difficult to conclude on this difference because, even if the same number of coatings have been carried out on both samples, YAG:Ce suspension deposition probably proceeds in a different way in the absence or in the presence of ZnO NWs, leading

to different amounts of YAG:Ce in the two samples. Indeed, deposition is expected to proceed by liquid spreading on the silicon substrate in the former case while it is governed by liquid impregnation through the NWs in the second case. Furthermore, liquid deposition can also be affected by differences in substrate properties such as surface tension or roughness, which will also influence the amount of YAG fixed on the substrate.

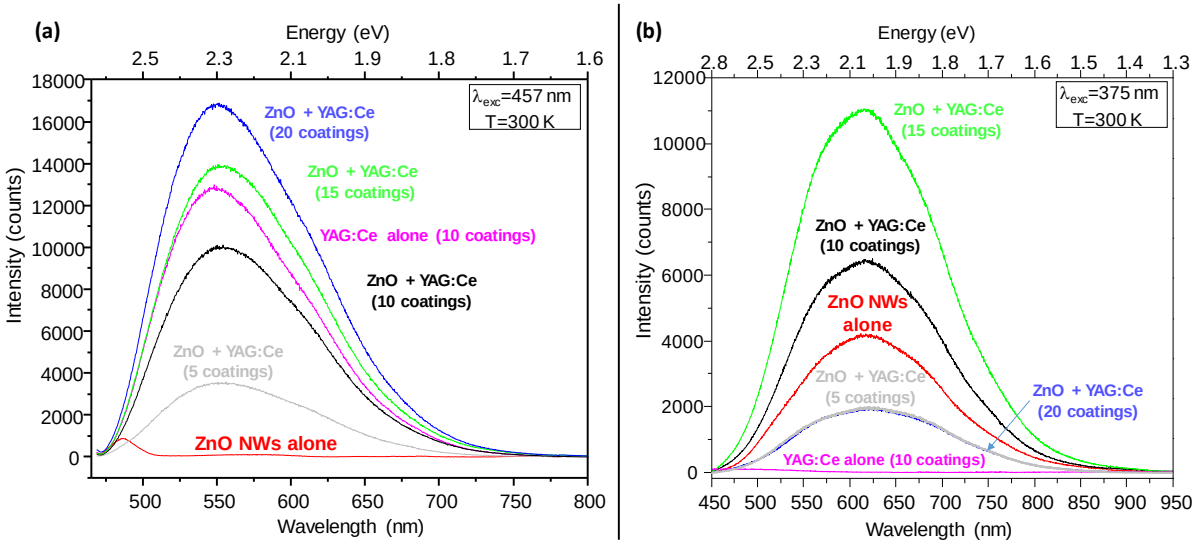


**Figure 9 : Room temperature emission spectra of ZnO NWs alone, YAG:Ce alone (10 coatings of 20 g/L ground YAG:Ce suspension) and ZnO/YAG:Ce composite coatings made with 5 to 20 impregnations of 20 g/L YAG:Ce NPs suspension (a) under blue and (b) UV excitations.**

Under UV excitation (Figure 9(b)) , emission spectra correspond to the visible emission of ZnO NWs: they consist of a very broad emission band from 450 to 850 nm peaking around 615 nm (2.02 eV). This emission signal can be deconvoluted into three Gaussian components (Figure 10) located at 557 nm/2.23 eV (20±1% of the total area), 626nm/1.98 eV (58±4%) and 697 nm/1.78 eV (22±5%). Even if there is a consensus that radiative recombination processes related to defects are responsible for this broad visible emission band, the exact origin of each contribution is still controversial. Since synthesis conditions and dimensionality of obtained ZnO greatly influence their defect landscape and so on their luminescence properties [11, 29, 52], the obtained emission profiles have been interpreted on the basis of several papers [11, 48, 53-55] dedicated to ZnO nanorods or nanowires elaborated by either hydrothermal method or electrochemical or physical vapor deposition. Both green-yellow ( 557 nm) and orange (626 nm) emissions involve double-ionized oxygen vacancies ($Vo^{++}$) and concern respectively transitions either from the conduction band (CB – around 3.36 eV) or from the interstitial Zn ($Zn_i$) whose energy levels lie between 0.05 and 0.5 eV below the conduction band [48, 53, 54]. The red emission (697 nm) is generally assigned to excess oxygen related defects ($O_i$ or zinc vacancies $V_{Zn}$) and in particular [48] to transitions from deeper $Zn_i$ ($Zn_i$*) to $O_i$ but some papers [54, 56] also ascribe it to $Zn_i^* \rightarrow Vo^{++}$ transitions. In our case, the predominance of the orange emission is concordant with the large surface to volume ratio of the nanorods since $Vo^{++}$ are known to nucleate preferentially at surfaces or grain boundaries [54, 55] or to originate from the recombination of $Vo^{+}$ defects and holes provided by the surface [57, 58]. It is important to underline the main orange-red component (between 615 and 800 nm) in these emission spectra since this color contribution is the one which has to be boosted in current solid-state lighting devices. The substantial

presence of oxygen vacancies and zinc interstitials, highlighted by their respective emissions signals, has been confirmed by Raman study as explained in SI (Figure S8 and its corresponding analysis).

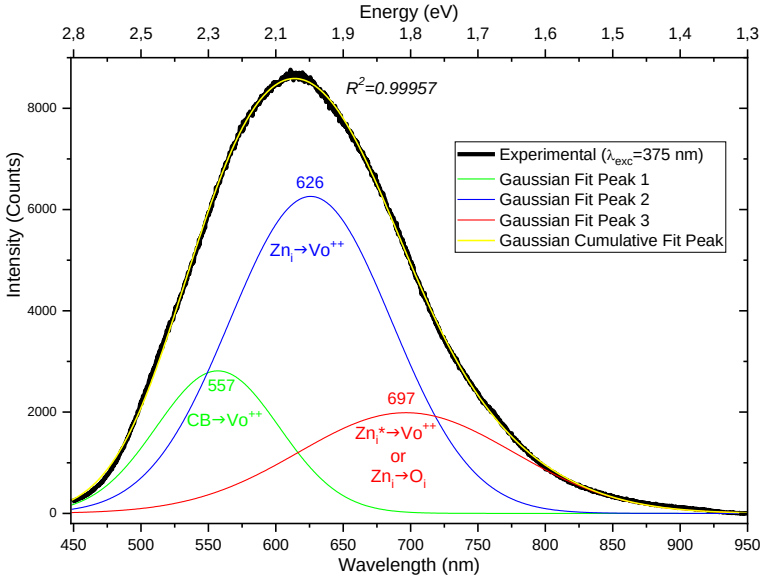


**Figure 10: Room temperature emission spectrum of ZnO NWs alone associated with its decomposition into three Gaussian components and their cumulative signal.**

Besides, Figure 9(b) shows that YAG:Ce alone does not present any significant emission line under 375 nm excitation, which is consistent with the excitation spectrum illustrated in Figure 8(b). However, in the presence of YAG:Ce NPs, emission intensity of ZnO NWs fluorescence drastically changes. To unravel such behavior, we have compared emission profiles in the absence and in the presence of YAG:Ce NPs to detect a spectral contribution of YAG:Ce luminescence in the form of a shoulder in the yellow region. Whatever the composite, emission profile remains the same as that recorded for ZnO NWs alone, only the emission intensity changes.

## 2.5. Photoluminescence mechanisms: discussion

In order to identify potential mechanisms explaining the behavior of composites under both 457 and 375 nm excitation, we have established a schematic energy diagram (Figure 11) based both on data derived from the literature[59, 60] and on deconvoluted emission spectra recorded under UV excitation (Figure 10). As illustrated on the Figure 11, an excitation wavelength of 457 nm could, at room temperature, entail an energy transfer from the $^2D_{3/2}$ level of $Ce^{3+}$ ions to the shallow levels of ZnO ($Zn_i/Zn_i^*$) from which radiative relaxation can occur to $Vo^{++}$ energy level, leading to orange-red emission. One can assume that this kind of mechanism takes place to a small extent under blue excitation, giving rise to the slight redshift of the emission maximum and to the expanse observed on the emission spectra the long wavelength side (Figure S7). A contribution of defect-related emission of ZnO has already been observed with ZnO NRs combined with a blue LED, also leading to a slight redshift of the electroluminescence peak position of the LED [14].

Under 375 nm excitation, regarding Figure 11, energy transfer might occur from CB of ZnO to $^2D_{3/2}$ level of $Ce^{3+}$ ions but this would entail significant changes in the emission profile shown in Figure 9(b) which is not the case. To further investigate the possibility of

such a mechanism and detect any energy transfer from ZnO NWs to $Ce^{3+}$ ions, decay curves of the red emission ($\lambda_{em}$=600 nm) of both ZnO NWs alone and YAG:Ce NPs/ZnO NWs composite (10 impregnations) have been recorded. Details about the fitting functions, decay curves and fitting parameters are presented in SI (Figure S9 and Table S1) as well as some secondary discussion. Decay curves can be fitted by bi-exponential functions and are characterized by rather similar time constants: $\tau_1$~0.38/0.40 ns and $\tau_2$~1.86/1.90 ns.

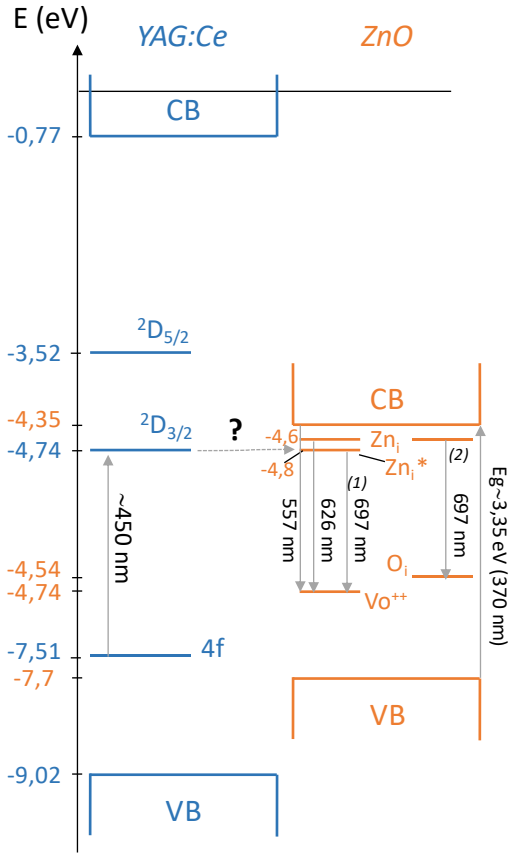


**Figure 11 : Schematic energy levels diagram based on one hand on the work of Merenga *et al.*[60] for YAG:Ce, and on the other hand both on the work of Tzeng *et al.* [59] and on the deconvoluted emission spectrum recorded in this work under 375 nm (Figure 10) for ZnO NWs.**

The main result is that decay profiles are similar with or without YAG:Ce and that no rise time is observed. It suggests there is no energy transfer between the radiative components that would have explained the enhancement of the emission intensity of ZnO signal in the presence of a certain amount of YAG:Ce NPs. We infer that such an energy transfer is unlikely to happen as a result of the very short non-radiative transitions from CB to shallow defects of ZnO whose time constant is much weaker than that of YAG:Ce (main characteristic decay time lying within the range 60-80 ns). Indeed, the whole mechanism of defect-related emission (non-radiative and radiative transitions) takes less than 10 ns as evidenced by the decay curves (Table 1).

Consequently, to explain the results obtained under 375 excitation, we guess that the observed trend arises from a competition between two main phenomena as illustrated in the schematic representations of the Figure 12. On the one hand, a direct excitation

of ZnO NWs by the UV source is likely to occur. Thanks to holes present at the NWs surface, oxygen vacancies are activated in the form of $Vo^{++}$ [11, 57], which can act as acceptors for electron-holes recombinations leading to visible defect-related ZnO emission. This emission is expected to occur directly from all parts of the NWs [11] but photons can also be extracted from YAG:Ce NPs. This light extraction is facilitated by the weaker refractive index of YAG:Ce ($n_{YAGbulk}$~1.8) compared to that of ZnO ($n_{ZnObulk}$~2.0-2.1) [12]. We can assume that the effective refractive index of YAG:Ce NPs remains lower than that of ZnO NWs arrays. This allows to reduce the gap between ZnO and the air ($n_{air}$~1) entailing a better light extraction *via* scattering effects through new or larger escape cones [2, 61] (Figure 12(a)). From that point of view, YAG:Ce NPs would not directly influence the luminescence emission (no effect on the emission profile) but would play a key role in its enhanced extraction, explaining the observed increase in emission intensity when the number of NPs impregnations grows from 5 to 15 (Figure 9(a)).

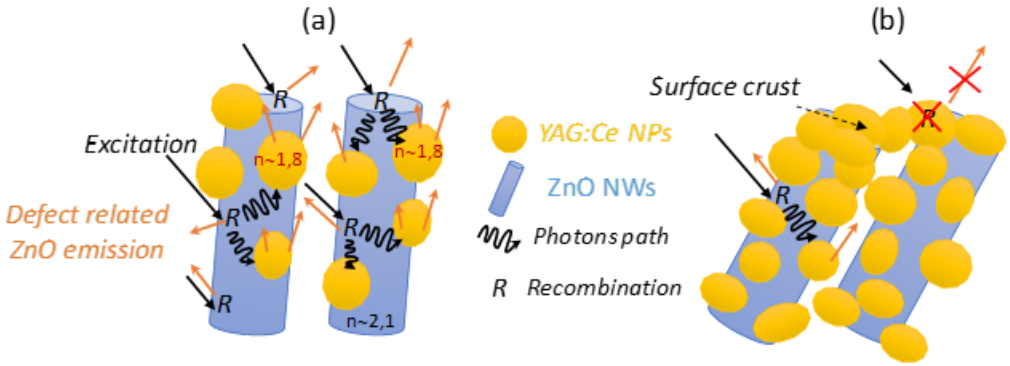


**Figure 12 : Schematic representation of the photons paths and associated emission mechanisms in the case of (a)10 and (b)20 impregnations with YAG:Ce NPs suspension**

However, when 20 impregnations are carried out, a thick YAG:Ce crust is formed which may have two consequences (Figure 12(b)): 1) it can act as a passivation shell for ZnO NWs preventing the activation of oxygen vacancies by screening the charge carriers located at the NWs surface and then inhibiting a major part of recombinations, as already observed using $Al_2O_3$ coating on ZnO nanorods [57, 62] and 2)this crust is likely to significantly shield the excitation signal. Both processes could account for the decrease in luminescence intensity after 20 impregnations. Furthermore, all described mechanisms can also explain why the signal measured after 5 impregnations is weaker than that measured for NWs alone. In that case, the measured intensity would diminish owing to a reduction in the number of charge carriers recombinations at the NWs surface and the amount of impregnated YAG:Ce NPs would be insufficient to counterbalance this reduction by promoting enhanced light extraction by scattering effects. In summary, all these descriptions can explain why, in our conditions, an optimal emission is measured after 15 impregnations for which the positive contribution of impregnated YAG:Ce NPs would be predominant.

Finally, based on the optical study of the elaborated architectures, these ones appear as very promising. Indeed, when overlapping the emission spectra obtained under UV and blue excitations, as illustrated in Figure 13, it becomes possible to flexibly tune the obtained light by playing on a mixture of both UV and blue LEDs in the same Printed Circuit Board (PCB). This provides key

opportunities to produce a white light with optimized photometric parameters (CRI, CTT for example) without the use of a red expensive and unreliable inorganic phosphor such as mentioned in the introduction.

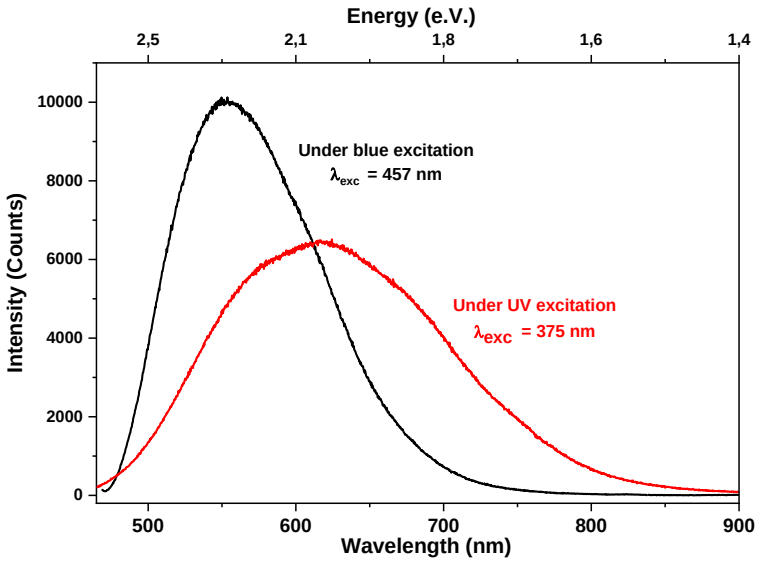


**Figure 13 : Room temperature emission spectra of a YAG :Ce/ZnO NWs composite coating prepared with 15 impregnations of ground YAG:Ce suspension.**

## CONCLUSIONS

ZnO NWs/YAG :Ce NPs functional heterostructure coatings have been elaborated for the first time using soft chemical processes. Even if YAG:Ce emission intensity has not been improved in the presence of ZnO NWs under blue excitation a slight change in emission profile has been evidenced, related to possible energy transfer from $Ce^{3+}$ ions to shallow defects of ZnO. Further experiments such as decay curves under blue excitation are required to totally confirm the occurrence of this energy transfer. Besides, a significant enhancement of visible emission of ZnO NWs (more than doubling) under near-UV excitation has been highlighted in the presence of YAG:Ce NPs. This enhancement has been assigned to a better extraction of photons emitted by the NWs thanks to YAG:Ce NPs which modify photons path thanks to the new escape cones they create. Furthermore, ZnO NWs/YAG :Ce NPs composites present the great advantage to be combinable with both blue and near-UV LEDs, giving rise to a tunable white light, which is generally obtained combining YAG:Ce with another expensive and unreliable inorganic red phosphor containing rare earths. Hence, this work paves the way to the use of this kind of original architecture to obtain more efficient and tunable LEDs-based devices using a cheap and eco-friendly material: ZnO. Further work will be dedicated to the use of transparent substrates and to their association with a PCB comprising near-UV and blue LEDs. These configurations will enable us to determine photometric parameters such as Color Rendering Index (CRI).

### Conflicts of interest

There are no conflict to declare.

## Acknowledgements

The authors are grateful to Christelle Blavignac, Claire Szczepaniak, Lorraine Novais Gameiro (Centre Imagerie Cellulaire Santé – Université Clermont Auvergne, France) and Arnaud Dalle (2Matech, Aubière, France) for their technical support and expertise for TEM and SEM observations respectively.

## Formatting of funding sources

This work was supported by the French Agence Nationale de la Recherche for its financial support in the frame of the ANR SMARtLEDs project (ANR-19-CE08-0001) and Campus France for the doctoral grant of Nehed Amara (grant 895161F).

## References

[1] V.K. Khanna, Fundamentals of Solid-State Lighting: LEDs, OLEDs, and Their Applications in Illumination and Displays, CRC Press, 2014.

[2] C. Geng, T. Wei, X. Wang, D. Shen, Z. Hao, Q. Yan, Enhancement of Light Output Power from LEDs Based on Monolayer Colloidal Crystal, Small, 10 (2014) 1668-1686.

[3] O.H. Kwon, J.W. Jang, S.-J. Park, J.S. Kim, S.J. Hong, Y.S. Jung, H. Yang, Y.J. Kim, Y.S. Cho, Plasmonic-Enhanced Luminescence Characteristics of Microscale Phosphor Layers on a ZnO Nanorod-Arrayed Glass Substrate, ACS Appl. Mater. Interfaces, 11 (2019) 1004-1012.

[4] Z. Li, K. Cao, J. Li, Y. Tang, L. Xu, X. Ding, B. Yu, Investigation of Light-Extraction Mechanisms of Multiscale Patterned Arrays With Rough Morphology for GaN-Based Thin-Film LEDs, IEEE Access, 7 (2019) 73890-73898.

[5] A. Lenef, A. Piquette, J. Kelso, Thermodynamics of Light Extraction from Luminescent Materials, ECS Journal of Solid State Science and Technology, 7 (2018) R3211-R3226.

[6] A.I. Zhmakin, Enhancement of light extraction from light emitting diodes, Phys. Rep., 498 (2011) 189-241.

[7] S.-F. Leung, Q. Zhang, F. Xiu, D. Yu, J.C. Ho, D. Li, Z. Fan, Light Management with Nanostructures for Optoelectronic Devices, J. Phys. Chem. Lett., 5 (2014) 1479-1495.

[8] H. Sun, A. Piquette, M. Raukas, T.D. Moustakas, Enhancement of yellow light extraction efficiency of $Y_3Al_5O_{12}$: $Ce^{3+}$ ceramic converters using a 2-D $TiO_2$ hexagonal-lattice nanocylinder photonic crystal layer, IEEE Photonics Journal, 8 (2016) 1-10.

[9] J.S. Kim, S.K. Eswaran, O.H. Kwon, S.J. Han, J.H. Lee, Y.S. Cho, Enhanced Luminescence Characteristics of Remote Yellow Silicate Phosphors Printed on Nanoscale Surface-Roughened Glass Substrates for White Light-Emitting Diodes, Advanced Optical Materials, 4 (2016) 1081-1087.

[10] D. Panda, T.-Y. Tseng, One-dimensional ZnO nanostructures: fabrication, optoelectronic properties, and device applications, J Mater Sci, 48 (2013) 6849-6877.

[11] A.B. Djurišić, Y.H. Leung, Optical Properties of ZnO Nanostructures, Small, 2 (2006) 944-961.

[12] H. Jeong, D.J. Park, H.S. Lee, Y.H. Ko, J.S. Yu, S.-B. Choi, D.-S. Lee, E.-K. Suh, M.S. Jeong, Light-extraction enhancement of a GaN-based LED covered with ZnO nanorod arrays, Nanoscale, 6 (2014) 4371-4378.

[13] H. Jeong, R. Salas-Montiel, G. Lerondel, M.S. Jeong, Ultraviolet, blue, and green InGaN-based light-emitting diodes functionalized with ZnO nanorods, J. Alloys Compd., 708 (2017) 612-618.

[14] C.B. Soh, C.B. Tay, S.J. Chua, H.Q. Le, N.S.S. Ang, J.H. Teng, Optimization of hydrothermal growth ZnO Nanorods for enhancement of light extraction from GaN blue LEDs, J. Cryst. Growth, 312 (2010) 1848-1854.

[15] H. Jeong, M.S. Jeong, Confocal electroluminescence investigations of highly efficient green InGaN LED via ZnO nanorods, J. Alloys Compd., 660 (2016) 480-485.

[16] Y.J. Park, H. Song, K.B. Ko, B.D. Ryu, T.V. Cuong, C.-H. Hong, Nanostructural Effect of ZnO on Light Extraction Efficiency of Near-Ultraviolet Light-Emitting Diodes, Journal of Nanomaterials, 2016 (2016) 6.

[17] M. Willander, O. Nur, S. Zaman, A. Zainelabdin, N. Bano, I. Hussain, Zinc oxide nanorods/polymer hybrid heterojunctions for white light emitting diodes, J. Phys. D: Appl. Phys., 44 (2011) 224017.

[18] S. Vempati, J. Mitra, P. Dawson, One-step synthesis of ZnO nanosheets: a blue-white fluorophore, Nanoscale research letters, 7 (2012) 470.

[19] Y. Zhang, A. Apostoluk, C. Theron, T. Cornier, B. Canut, S. Daniele, B. Masenelli, Doping of ZnO inorganic-organic nanohybrids with metal elements, Scientific Reports, 9 (2019) 11959.

[20] H. Li, W. Zhao, Y. Liu, Y. Liang, L. Ma, M. Zhu, C. Yi, L. Xiong, Y. Gao, High-level-Fe-doped P-type ZnO nanowire array/n-GaN film for ultraviolet-free white light-emitting diodes, Mater. Lett., 239 (2019) 45-47.

[21] A. Layek, P.C. Stanish, V. Chirmanov, P.V. Radovanovic, Hybrid ZnO-Based Nanoconjugate for Efficient and Sustainable White Light Generation, Chem. Mater., 27 (2015) 1021-1030.

[22] Z. Xia, Z. Xu, M. Chen, Q. Liu, Recent developments in the new inorganic solid-state LED phosphors, Dalton Trans., 45 (2016) 11214-11232.

[23] L. Wang, R.-J. Xie, T. Suehiro, T. Takeda, N. Hirosaki, Down-Conversion Nitride Materials for Solid State Lighting: Recent Advances and Perspectives, Chem. Rev., 118 (2018) 1951-2009.

[24] R. Boonsin, G. Chadeyron, J.-P. Roblin, D. Boyer, R. Mahiou, Development of rare-earth-free phosphors for eco-energy lighting based LEDs, J. Mater. Chem. C, 3 (2015) 9580-9587.

[25] Q. Zhou, L. Dolgov, A.M. Srivastava, L. Zhou, Z. Wang, J. Shi, M.D. Dramićanin, M.G. Brik, M. Wu, $Mn^{2+}$ and $Mn^{4+}$ red phosphors: synthesis, luminescence and applications in WLEDs. A review, J. Mater. Chem. C, 6 (2018) 2652-2671.

[26] X. Liu, X. Wang, H. Li, L. Pan, T. Lv, Z. Sun, C. Sun, Microwave-assisted synthesis of ZnO–$Y_3Al_5O_{12}$:$Ce^{3+}$ composites with enhanced visible light photocatalysis, J. Mater. Chem., 22 (2012) 16293-16298.

[27] L. Zammouri, A. Aboulaich, B. Capoen, M. Bouazaoui, M. Sarakha, M. Stitou, R. Mahiou, Synthesis of YAG:Ce/ZnO core/shell nanoparticles with enhanced UV-visible and visible light photocatalytic activity and application for the antibiotic removal from aqueous media, J. Mater. Res., 34 (2019) 1318-1330.

[28] K. Chao, Z. Xiao, H. Zhang, W. Niu, W. Xia, S. Sang, Y. Xin, Q. Li, S. Wu, S. Zhang, The surface coating of YAG:Ce phosphors with ZnO nanoparticles for white LED, Mater. Sci. Forum, 675-677 (2011) 1283-1286.

[29] E.G. Barbagiovanni, V. Strano, G. Franzò, R. Reitano, A.S. Dahiya, G. Poulin-Vittrant, D. Alquier, S. Mirabella, Universal model for defect-related visible luminescence in ZnO nanorods, RSC Adv., 6 (2016) 73170-73175.

[30] T. Demes, C. Ternon, D. Riassetto, H. Roussel, L. Rapenne, I. Gélard, C. Jimenez, V. Stambouli, M. Langlet, New insights in the structural and morphological properties of sol-gel deposited ZnO multilayer films, J. Phys. Chem. Solids, 95 (2016) 43-55.

[31] T. Demes, C. Ternon, D. Riassetto, V. Stambouli, M. Langlet, Comprehensive study of hydrothermally grown ZnO nanowires, J Mater Sci, 51 (2016) 10652-10661.

[32] T. Demes, C. Ternon, F. Morisot, D. Riassetto, M. Legallais, H. Roussel, M. Langlet, Mechanisms involved in the hydrothermal growth of ultra-thin and high aspect ratio ZnO nanowires, Appl. Surf. Sci., 410 (2017) 423-431.

[33] N. Pradal, G. Chadeyron, A. Potdevin, J. Deschamps, R. Mahiou, Elaboration and optimization of Ce-doped $Y_3Al_5O_{12}$ nanopowder dispersions, J. Eur. Ceram. Soc., 33 (2013) 1935-1945.

[34] K. Kodama, T. Uchino, Variations in Decay Rate of Green Photoluminescence in ZnO under Above- and Below-Band-Gap Excitation, J. Phys. Chem. B, 118 (2014) 23977-23985.

[35] Y. Ren, Z. Yuan, J. Fan, W. Huang, C. Shuai, Annealing temperature-dependent morphology, structure, and optical properties of well-aligned ZnO nanowire arrays, Applied Physics A, 124 (2018) 655.

[36] Y. Sun, X. Gu, Y. Zhao, L. Wang, Y. Qiang, Temperature-dependent photoluminescence analysis of ZnO nanowire array annealed in air, Superlattices Microstruct., 117 (2018) 520-526.

[37] T. Ekström, C. Chatfield, W. Wruss, M. Maly-Schreiber, The use of X-ray diffraction peak-broadening analysis to characterize ground Al2O3 powders, J Mater Sci, 20 (1985) 1266-1274.

[38] B. Lönnberg, Characterization of milled $Si_3N_4$ powder using X-ray peak broadening and surface area analysis, J Mater Sci, 29 (1994) 3224-3230.

[39] A.A. Othman, M.A. Osman, A.G. Abd-Elrahim, The effect of milling time on structural, optical and photoluminescence properties of ZnO nanocrystals, Optik, 156 (2018) 161-168.

[40] R.E. Rojas-Hernandez, F. Rubio-Marcos, E. Enríquez, M.A. De La Rubia, J.F. Fernandez, A low-energy milling approach to reduce particle size maintains the luminescence of strontium aluminates, RSC Adv., 5 (2015) 42559-42567.

[41] V. Havasi, D. Tátrai, G. Szabó, E. Varga, A. Erdőhelyi, G. Sipos, Z. Kónya, Á. Kukovecz, On the effects of milling and thermal regeneration on the luminescence properties of Eu2+ and Dy3+ doped strontium aluminate phosphors, J. Lumin., 219 (2020) 116917.

[42] S. Mishra, A. Khare, S. Tiwari, D.S. Kshatri, Diminution in photoluminescent intensity of SrS: Ce3+ phosphor due to increased milling time, J. Alloys Compd., 695 (2017) 1956-1965.

[43] G. Blasse, B.C. Grabmaier, Luminescent Materials, Springer-Verlag, Berlin, 1994.

[44] P. Dorenbos, 5d-level energies of Ce3+ and the crystalline environment. IV. Aluminates and "simple" oxides, J. Lumin., 99 (2002) 283-299.

[45] S. Nakamura, S. Pearton, G. Fasol, The Blue Laser Diode: The Complete Story, 2nd updated and extended ed., Springer, Berlin, 2000.

[46] B.L. Abrams, P.H. Holloway, Role of the Surface in Luminescent Processes, Chem. Rev., 104 (2004) 5783-5802.

[47] H. Terraschke, C. Wickleder, UV, Blue, Green, Yellow, Red, and Small: Newest Developments on Eu2+-Doped Nanophosphors, Chem. Rev., 115 (2015) 11352-11378.

[48] E.G. Barbagiovanni, R. Reitano, G. Franzò, V. Strano, A. Terrasi, S. Mirabella, Radiative mechanism and surface modification of four visible deep level defect states in ZnO nanorods, Nanoscale, 8 (2016) 995-1006.

[49] P. Camarda, F. Messina, L. Vaccaro, S. Agnello, G. Buscarino, R. Schneider, R. Popescu, D. Gerthsen, R. Lorenzi, F.M. Gelardi, M. Cannas, Luminescence mechanisms of defective ZnO nanoparticles, Phys. Chem. Chem. Phys., 18 (2016) 16237-16244.

[50] J. Shmulovich, G.W. Berkstresser, D. Brasen, Tb3+→Ce3+ energy transfer in Tb3+:Ce3+:YAG single crystalsa), J. Phys. Chem., 82 (1985) 3078-3082.

[51] L.-C. Chen, C.-C. Huang, Optoelectronic characteristics of YAG phosphor-incorporated ZnO films deposited by ultrasonic spray pyrolysis, Nanoscale Research Letters, 7 (2012) 627.

[52] K. Mahmood, S.B. Park, H.J. Sung, Enhanced photoluminescence, Raman spectra and field-emission behavior of indium-doped ZnO nanostructures, J. Mater. Chem. C, 1 (2013) 3138-3149.

[53] C. Park, J. Lee, W.S. Chang, Geometrical Separation of Defect States in ZnO Nanorods and Their Morphology-Dependent Correlation between Photoluminescence and Photoconductivity, J. Phys. Chem. B, 119 (2015) 16984-16990.

[54] K. Bandopadhyay, J. Mitra, Zn interstitials and O vacancies responsible for n-type ZnO: what do the emission spectra reveal?, RSC Adv., 5 (2015) 23540-23547.

[55] Z.-M. Liao, H.-Z. Zhang, Y.-B. Zhou, J. Xu, J.-M. Zhang, D.-P. Yu, Surface effects on photoluminescence of single ZnO nanowires, Phys. Lett. A, 372 (2008) 4505-4509.

[56] A.B. Djurišić, Y.H. Leung, K.H. Tam, L. Ding, W.K. Ge, H.Y. Chen, S. Gwo, Green, yellow, and orange defect emission from ZnO nanostructures: Influence of excitation wavelength, Appl. Phys. Lett., 88 (2006) 103107.

[57] J.P. Richters, T. Voss, D.S. Kim, R. Scholz, M. Zacharias, Enhanced surface-excitonic emission in ZnO/Al2O3 core–shell nanowires, Nanotechnology, 19 (2008) 305202.

[58] T.J. Penfold, J. Szlachetko, F.G. Santomauro, A. Britz, W. Gawelda, G. Doumy, A.M. March, S.H. Southworth, J. Rittmann, R. Abela, M. Chergui, C.J. Milne, Revealing hole trapping in zinc oxide nanoparticles by time-resolved X-ray spectroscopy, Nature Communications, 9 (2018) 478.

[59] L.-J. Tzeng, C.-L. Cheng, Y.-F. Chen, Enhancement of band-edge emission induced by defect transition in the composite of ZnO nanorods and CdSe/ZnS quantum dots, Opt. Lett., 33 (2008) 569-571.

[60] H. Merenga, J. Andriessen, C.W.E. Van Eijk, Positions of 4f and 5d energy levels of Ce3+ in the band gap of CeF3, YAG and LSO, Radiat. Meas., 24 (1995) 343-346.

[61] C.-Y. Fang, Y.-L. Liu, Y.-C. Lee, H.-L. Chen, D.-H. Wan, C.-C. Yu, Nanoparticle Stacks with Graded Refractive Indices Enhance the Omnidirectional Light Harvesting of Solar Cells and the Light Extraction of Light-Emitting Diodes, Adv. Funct. Mater., 23 (2013) 1412-1421.

[62] C. Chen, H. He, Y. Lu, K. Wu, Z. Ye, Surface Passivation Effect on the Photoluminescence of ZnO Nanorods, ACS Appl. Mater. Interfaces, 5 (2013) 6354-6359.